Fast-spin-echo versus rapid gradient-echo for 3D magnetization-prepared acquisitions: Application to inhomogeneous magnetization transfer

Manuel Taso, Fanny Munsch, Olivier Girard, Guillaume Duhamel, David Alsop, Gopal Varma

Fast-Spin-Echo versus Rapid Gradient-Echo for 3D Magnetization-Prepared acquisitions: application to Inhomogeneous Magnetization Transfer (ihMT)

Manuel Taso[1], Fanny Munsch[1], Olivier M. Girard[2], Guillaume Duhamel[2], David C. Alsop[1] and Gopal Varma[1]

[1] *Division of MRI Research, Department of Radiology, Beth Israel Deaconess Medical Center and Harvard Medical School, Boston, MA*

[2] *Aix-Marseille Univ, CNRS, CRMBM, Marseille, France*

Corresponding author

Manuel Taso, Ph.D.

Beth Israel Deaconess Medical Center

Division of MRI Research – Dept. of Radiology

330, Brookline Avenue – Ansin 244

Boston, MA 02215

mtaso@bidmc.harvard.edu

+1 (617) 667-0290

Number of words: 5114

Number of tables and figures: 10

Key-words: inhomogeneous magnetization transfer, Fast-Spin-Echo, myelin imaging, Signal to Noise, volumetric imaging

Abstract

Purpose: To evaluate the benefits of Fast Spin Echo (FSE) imaging over Rapid Gradient-Echo (RAGE) for Magnetization-prepared inhomogeneous Magnetization Transfer (ihMT) imaging.

Methods: A 3D FSE sequence was modified to include an ihMT preparation (ihMT-FSE) with an optional CSF suppression based on an Inversion-Recovery (ihMT-FLAIR). After numerical simulations assessing SNR benefits of FSE and the potential impact of an additional inversion-recovery, ihMT-RAGE, ihMT-FSE and ihMT-FLAIR sequences were compared in a group of 6 healthy volunteers, evaluating image quality, thermal and physiological noise as well as quantification using an ihMTsat approach. A preliminary exploration in the cervical spinal cord was also conducted in a group of 3 healthy volunteers.

Results: Several fold improvement in thermal SNR was observed with ihMT-FSE in agreement with numerical simulations. However, we observed significantly higher physiological noise in ihMT-FSE compared to ihMT-RAGE that was mitigated in ihMT-FLAIR, which provided the best total SNR (+74% and 49% compared to ihMT-RAGE in the white and gray matter, $p \leq 0.004$). IhMTsat quantification was successful in all cases with strong correlation between all sequences ($r^2 > 0.75$). Early experiments showed potential for spinal cord imaging.

Conclusions: FSE generally offers higher SNR compared to gradient-echo based acquisitions for magnetization-prepared contrasts as illustrated here in the case of ihMT. However, physiological noise has a significant effect, but an IR-based CSF suppression was shown to be efficient in mitigating effects of CSF motion.

Introduction

Three-dimensional (3D) encoding has significant advantages for Magnetic Resonance Imaging. The higher Signal-to-Noise Ratio (SNR) compared to 2D sequential encoding combined with increased spatial coverage allows high-resolution, often isotropic, imaging of entire organs in a single acquisition.

Short TR gradient-echo readouts (e.g. MPRAGE or SSFP) are advantageous for 3D imaging (1) because of their speed and good image quality. However, multiple spin-echo imaging has a fundamental advantage over spoiled gradient-echo in terms of SNR thanks to the use of a 90-degree excitation pulse followed by higher refocusing flip-angles. Nonetheless, multiple spin-echo based acquisitions are substantially slower than Echo-Planar Imaging, even with Fast-Spin-Echo (FSE) imaging (2). The development of variable flip-angle FSE (2–5) allowing long echo-train acquisition with reduced T_2-blurring and power deposition (and thus SAR), combined with parallel-imaging acceleration capabilities, offer new possibilities for faster 3D FSE imaging. Commercial implementations (Cube, SPACE, VISTA) have become extremely popular (6) for high-resolution anatomical imaging of the central nervous system (e.g. brain and spinal cord). They are increasingly used in combination with various magnetization preparations such as Arterial Spin Labeling perfusion (7) and Chemical Exchange Saturation Transfer (CEST) imaging (8) in the brain as well as in the body.

Inhomogeneous Magnetization Transfer (ihMT) is a recent MRI technique whose endogenous contrast (9) has shown great promise for myelin imaging in the central

nervous system (10). This technique exploits dipolar order effects induced by single frequency off-resonance saturation that are accentuated in tissues with a characteristically long dipolar order relaxation time, $T_{1,D}$ (11,12), as is the case in myelinated tissues (13). Detecting dipolar order effects with ihMT relies on the difference between acquisitions following single and dual off-resonance radiofrequency (RF) irradiation with equal power (7). As a relatively new contrast mechanism, the focus on ihMT has included theoretical characterization of the ihMT signal (14,15), development of analytical models (12,14), and applications in healthy (16–19) as well as diseased (20–22) central nervous system tissues (brain and spinal cord). As often occurs for the initial study of novel contrasts, early ihMT implementations relied on fast and robust single-slice imaging sequences such as Echo-Planar-Imaging (EPI) (9,23) and Single-Shot Fast-Spin-Echo (24,25). While these sequences are extremely appropriate for early developments, troubleshooting, and pioneering applications, their shortcomings limit wider adoption and use, especially for clinical studies. In the case of ihMT, 3D volumetric sequences were developed and implemented for brain imaging, relying on Gradient-Echo implementations (26–29) and recently Ultrashort Echo Time (UTE) sequences (30).

The modest signal change encountered with ihMT (<10% of the fully-relaxed magnetization) makes high SNR 3D readouts particularly desirable. Consequently, we explored the possibility of using 3D FSE sequences for ihMT, but early observations showed that while the potential for increased SNR was confirmed, we could also observe significant physiological noise contribution from CSF motion (31). Here we report in detail the implementation of a 3D FSE sequence for ihMT imaging of the brain

as well as an inversion-recovery based CSF-suppression variant referred to as ihMT-FLAIR. After theoretical simulations to assess the effect of an inversion-recovery based CSF suppression strategy on the ihMT signal, we show in-vivo results, and compare ihMT-FSE and ihMT-FLAIR image quality and quantification to a gradient-echo based acquisition (i.e. ihMT-RAGE), with quantification using a modified MTsat framework (32). A particular emphasis is set on assessing different noise sources and their relative distribution across the different 3D sequences to provide a detailed SNR assessment. We also demonstrate the feasibility of CSF-suppressed 3D ihMT with FSE in the spinal cord.

Methods

- **Sequence design**

The magnetization preparation for ihMT experiments using an FSE readout is illustrated in Figure 1. We employed a low duty-cycle ihMT saturation (23) because it creates a larger ihMT signal within a chosen RF power deposition limit compared to early, higher duty cycle implementations. Briefly, the ihMT preparation uses, for the single-offset saturation, a train of 5 ms Tukey shaped RF pulses with peak $B_{1,ihMT}$ applied at an offset frequency of either + 7kHz or -7kHz every $ihMT_{TR}$ for a saturation time T_{ihMT} (with T_{ihMT} = N-1 * $ihMT_{TR}$ with N the number of pulses). For dual frequency irradiation, cosine-modulation of the 5 ms Tukey shaped RF pulses was used with peak B1 amplitude of $\sqrt{2}$ * $B_{1,ihMT}$. An optional spatially non-selective adiabatic inversion pulse positioned at an inversion time TI optimized for nulling CSF signal at excitation time was implemented and referred to as ihMT-FLAIR. This inversion was achieved with a C-shaped FOCI (33), applied with peak B_1 = 14 uT, pulse width = 15.36 ms and bandwidth = 10.8 kHz. The TI was determined by estimating the CSF signal as given by the following equation:

$$S(TI) = S_0.\left(1 - 2.e^{-\frac{TI}{T_{1,CSF}}} + e^{\frac{-(TR_{FSE}-TE_{last})}{T_{1,CSF}}}\right) \quad (1)$$

With $T_{1,CSF}$ = 4000 ms, TR_{FSE} = 6 s and TE_{last} = 408 ms (for an ETL of 130 and echo-spacing of 3.1 ms). After a wait time T_{wait}, the ihMT preparation as described above is applied.

Following the ihMT preparation, a variable flip-angle (VFA) FSE readout is played out starting with a non-selective 90 degree excitation followed by a train of VFA hard pulses. In the current work, the default VFA scheme implemented in the product VFA 3D-FSE sequence was used (Cube, GE Healthcare), with an initial 120 degrees refocusing FA, rapid decrease to 50 degrees at the 6th echo followed by a gradual increase back to 120 degrees at the end of the train, as illustrated in Supporting Information Figure S1. Four echoes were discarded at the beginning of the train for stabilization purposes. A centric-out, radial fan-beam view ordering was used for minimal T_2-weighting leading to an effective TE=15.5 ms. Although standard for relatively short TR imaging with Fast-Spin-Echo, the driven-equilibrium 90-degree flip-back pulse was explicitly removed as preliminary experiments showed a detrimental effect on motion-sensitivity. A full dummy acquisition scheme including one TR of each saturation scheme (ihMT preparation and FSE readout) was played out prior to data acquisition, leading to 4*TR dummy scan.

An interleaved acquisition of different saturation schemes was implemented. Single-positive, dual frequency, single-negative and another dual frequency saturation were sequentially acquired with the same phase encoding of the echo train before changing to the next phase encoding interleave to minimize motion-sensitivity. The acquisition of two dual frequency volumes allowed calculation of a temporal standard deviation in addition to increasing SNR. Although it was previously reported that an interleaved saturation scheme led to lower ihMT signal for a short TR gradient-echo based acquisition (27), this effect should be reduced for the longer TR employed for ihMT-FLAIR. Additionally, in both ihMT-FSE and ihMT-FLAIR acquisitions, three successive

90 degrees quadratic phase saturation pulses (10 ms width, 12.5 kHz bandwidth) were played every 17ms after the end of the FSE readout using varying gradient direction crushers once in each orthogonal direction, of nominal amplitude 19 mT/m and varying RF phase.

- **Numerical simulations**

We used a previously described model (23,34) by modifying code available at https://github.com/gvarma617/ihMTRAGE-optimize to simulate the effect of a preparatory inversion on the ihMT signal. The CSF suppression was modeled as an instantaneous and full inversion of the free pool (i.e. assuming perfect inversion efficiency), effectively changing the initial magnetization condition in the white and gray matter to account for T_1-recovery after the inversion, assuming in grey matter (GM) $T_{1,GM}$ = 1818 ms and in white matter (WM) $T_{1,WM}$ = 1087 ms (35) at 3T. We compared the difference in longitudinal magnetizations as a measure of ihMT ($ihMT_z$) with and without the non-selective IR at T=0 (prior to the first excitation pulse, e.g. TI in the case of ihMT-FLAIR). We also calculated ihMT after simulating a single, instantaneous excitation pulse (ihMT signal) of either 10 or 90 degrees corresponding to experimental RAGE or FSE acquisitions, defined as ihMT signal = ihMTz . sin(α). A dummy segment was simulated (including preparation, acquisition and delays) to reach a steady-state. Furthermore, we assessed the potential effect of the non-selective inversion on the bound pool, by varying the longitudinal magnetization of the bound pool (based on its value at thermal equilibrium $M_{0,b}$) from $-M_{0,b}$ to $+M_{0,b}$ following simulated inversion and

calculating the ihMT ratio (ihMTR) for white and gray matter. For ihMTR simulation (=ihMTsignal/$M_{z,0}$), we also simulated the zero power longitudinal magnetization $M_{z,0}$.

- **Experiments**

All experiments were performed on a 3T scanner (Discovery MR750, GE Healthcare, Waukesha, WI) using body-coil RF transmission and a 32-channel receive-only head array or an 8-channel Cervical Thoracic Lumbar receive array for spine applications. We scanned a total of 9 healthy volunteers with N=6 for brain experiments (4 males, 2 females, 33 ± 8 y.o) and N=3 for cervical spinal cord experiments (37 ± 6yo, all males). All volunteers provided written informed consent prior to scanning, and this study was approved by our institutional Committee on Clinical Investigations. All experiments were carried out in First-level operating mode for SAR and dB/dt management under FDA guidelines (6min-averaged head SAR < 3.2 W/kg). Total imaging time was < 1 hour. The 6min-averaged head SAR recorded by the power monitor was saved for comparison between the different sequences.

In all scans, the same ihMT preparation (excluding inversion pulse) was used, with $ihMT_{TR}$ = 100ms, total saturation time T_{ihMT} = 900 ms (N=10 pulses) peak $B_{1,ihMT}$ = 12 uT for a single-frequency pulse. A complete saturation scheme consisted of one zero-power reference scan as well as 4 MT acquisitions: single positive offset, dual offset, single negative offset, and then another dual offset RF saturation.

Spatial coverage as well as nominal resolution was kept constant throughout all scans (96x96 matrix, 64 sagittal slices, 2.4 x 2.4 x 2.8 mm^3 spatial resolution). Additionally, parallel-imaging acceleration was used in all cases with autocalibrating reconstruction (ARC, GE Healthcare) and the same acceleration factor of R=2 in both phase and slice directions.

We acquired ihMT-FLAIR, ihMT-FSE and ihMT-RAGE data, as implemented in Varma et al. (27) in each volunteer. Detailed parameters are provided in Table 1. While having very different characteristics, all acquisitions were optimized to be closely matched in terms of scan time and imaging parameters, especially key parameters affecting SNR such as receiver bandwidth.

For both FSE and RAGE, an additional single repetition with no RF power applied in both preparation and readout was acquired to estimate thermal noise as detailed below with the same receive bandwidth and receiver gain for the ihMT and noise-only volumes. All ihMT data were saved as raw k-space data.

In addition to the ihMT data, in 5 of the volunteers for brain experiments, we also acquired MP2RAGE (36) volumes for quantitative T_1 imaging (1.6mm isotropic, $TR_{MP2RAGE}$ = 4.5s, TI_1 / TI_2 = 700 / 2000 ms, α_1 / α_2 = 4 / 5 degrees), as well as a transmit field (B_1) map using a low-resolution RF-spoiled Bloch-Siegert sequence to support quantification as detailed later.

For spinal cord experiments, after anatomical 3D sagittal T_2-weighted FSE and axial T_2*-weighted multi-echo gradient-echo sequences, ihMT-FLAIR images were acquired

in the axial orientation, targeting the upper cervical spinal cord (centered on C3), using the same preparation parameters except for the total saturation time T_{ihMT}=1400ms for increased sensitivity because of lower expected SNR. A slab-selective excitation with flow-compensation using first-moment gradient nulling in the frequency direction was employed. Imaging parameters were: TI / TR / TE = 2000 / 6000 / 14 ms, 160x160 matrix, 5-mm slice thickness, nominal in-plane resolution 1.2x1.2 mm^2. No cardiac gating was used. The number of slices was adjusted based on the spine curvature to acquire as many slices uncorrupted by partial volume effect in the slice direction. Two repetitions of the saturation scheme were acquired in 12 minutes.

- **Image reconstruction and analysis**

IhMT data reconstruction

All image reconstruction was performed with custom made MATLAB scripts (R2020a, The MathWorks, Natick, MA).

IhMT-RAGE, ihMT-FSE and ihMT-FLAIR k-space data were reconstructed by first estimating coil-sensitivities using a direct auto-calibration (37) method followed by parallel-imaging reconstruction. This was performed using the Berkeley Advanced Reconstruction Toolbox (BART) (38) with the 'caldir' command, using a 24^2 central k-space region.

To account for the T_2-decay during the long FSE echo-train, an echo-train scaling was performed to act as a deblurring k-space filter (39) assuming T_1=1250ms and T_2=80ms (intermediate between white and gray matter). This scaling was designed to achieve a

Tukey-window (with a r=0.75 cosine fraction) to balance deblurring with SNR loss and was performed prior to the FSE reconstruction. Practically, the theoretical (e.g. assuming perfect B_1) echo amplitude evolution was simulated with an Extended Phase Graph (EPG) algorithm (40) for the T_1/T_2 mentioned. Then, for each echo and therefore k-space position, a scaling factor was calculated to reach the target window as illustrated in Supporting Information Figure S2. This filter was applied to both ihMT and noise datasets.

For each subject, we performed an intra-subject registration of individual MT-weighted volumes for motion-correction using SPM12 (Wellcome Trust Center for Neuroimaging, London, UK). The ihMT difference volumes were computed from reconstructed images as follows:

$$ihMT_{diff} = S_{+} + S_{-} - (S_{dual,1}+S_{dual,2}) \quad (2)$$

With S_{+}, S_{-}, and $S_{dual,1}$, $S_{dual,2}$ the data acquired following single positive, single negative, and dual frequency MT preparations.

We estimated an experimental Point-Spread-Function (PSF) using a blind deconvolution method (41,42) in both phase and slice-encoding directions.

Additionally, ihMT-RAGE, ihMT-FSE and ihMT-FLAIR group averages were built using the Advanced Normalization Toolbox (ANTs) multivariate template construction framework (43) (BSpline-SyN transformation, cross-correlation metric, 4 outer iterations, Laplacian sharpening), to provide a visual assessment of image quality at the group level.

Signal and noise considerations

SNR calculation is always challenging when using multi-array coils and parallel-imaging reconstructions. We therefore used the pseudo-replica method as proposed by Robson et al. (44) to overcome this issue. The noise-only k-space data was used to estimate a noise covariance matrix followed by random generation of correlated noise (as implemented in *http://hansenms.github.io/sunrise/sunrise2013/*).

This random correlated noise was then added to the ihMT subtracted k-space and the process was repeated 100 times. A noise-only image (named rSD) was then generated by calculating a pixel-wise standard deviation across the replicas. The process is illustrated in Figure 2.

In addition, in order to measure the total of physiologic and thermal noise amplitude and distribution, we calculated for each acquisition a pixel-wise temporal standard deviation (tSD) of the dual frequency volumes as these are acquired twice in the ihMT-FLAIR datasets (number of repetitions equals 1), and four times for ihMT-FSE and ihMT-RAGE (number of repetitions equals 2).

We then calculated a signal to noise ratio due to thermal and other random sources unrelated to the image intensity (SNR_{rand}) in both WM and GM by using whole-brain WM and GM segmentations and dividing the mean signal in the ihMT difference image by the random noise-only image (rSD) in the same ROI. This was done for the ihMT-RAGE, ihMT-FLAIR and ihMT-FSE.

We also calculated in the same ROIs a ratio of the temporal SD to random noise (tSD / rSD) by dividing the mean of the temporal SD of dual frequency saturation volumes by

the mean of the random noise image. This ratio reflects the relative contribution of physiological and thermal noise of reconstructed images.

A total SNR map (SNR_{tot}) was computed and values were calculated in the same GM/WM ROI (SNR_{tot}) by dividing the ihMT difference image by the tSD as this includes all sources of noise.

In both SNR_{tot} and SNR_{rand}, as the noise image was only acquired once and because of noise propagation through the ihMT calculation, the noise signal had to be scaled by a factor of $\sqrt{N}$ (divided by 2 in the case of RAGE/FSE because of the division used in the ihMT calculation), N being the number of images used for ihMT calculation. This led to scaling by a factor of $\sqrt{2}$ ($=\sqrt{8}/2$) for ihMT-RAGE and ihMT-FSE and by 2 ($=\sqrt{4}$) in ihMT-FLAIR.

We also derived a contrast measure defined as Michelson's Contrast:

$$C = [ihMTdiff(WM) - ihMTdiff(GM)]/[ihMTdiff(WM) + ihMTdiff(GM)] \quad (3)$$

Pairwise comparisons of SNR_{rand}, tSD / rSD, SNR_{tot} and C were performed using paired t-tests assuming unequal variances, with a significance set at $p<0.05$.

Quantification of ihMT parameters using ihMTsat

In order to provide a quantitative ihMT metric immune to B_1+ and T_1 that could be compared across all three sequences, we used in 5 of the 6 volunteers a previously proposed adaptation of MTsat quantification (32) for ihMT to estimate an ihMTsat parameter (45). Briefly, this method quantifies the signal attenuation due to a single off-resonance RF pulse on the free pool (referred to as MTsat, δ_{MT}) which allows disentangling MT from confounding factors, providing a metric independent of B1+ and

T1, if the exchange rate is fast compared to the pulse repetition rate. In the case of ihMT, this is performed for both single and dual frequency saturation and an ihMTsat parameter can be calculated as:

$$ihMTsat = 2*\delta_{MT,dual}-\delta_{MT+}-\delta_{MT-} \quad (4)$$

The ihMTsat parameter therefore represents the difference between the fraction of free-pool water saturated with either a dual or single frequency saturation.

The full model is detailed in the Appendix of Munsch et al. (19) and the FLAIR adaptation is presented in the Appendix at the end of the current study. In this study the T_1 map derived from the MP2RAGE sequence was used in the quantification.

For ihMT-FLAIR, we modified the physical model from (19) to account for full and instantaneous inversion of the free pool by the non-selective inversion (assuming perfect inversion efficiency) and assuming zero net longitudinal magnetization at the end of the FSE imaging readout of 400ms.

In both FSE/FLAIR cases, we also included the post-readout recovery time. Individual saturations and zero-power volumes were smoothed using a Gaussian kernel (σ = 1x1x1 voxel) prior to ihMTsat quantification to avoid aberrant values due to CSF signal in FSE acquisitions leading to sharp intensity transitions.

Pearson correlation coefficients as well as Bland-Altman plots were computed between ihMTsat values from the ihMT-RAGE, ihMT-FSE and ihMT-FLAIR. This was done in ROIs derived from the Harvard cortical and subcortical atlases for GM and JHU atlas for WM after spatial normalization to the MNI_{152} template.

Spinal cord data reconstruction

Spinal cord ihMT difference volumes were computed after performing a motion-correction, achieved with the Spinal Cord Toolbox (46) with a segmentation-based registration of all MT volumes to the first zero-power volume.

Results

- **Numerical simulations**

Figure 3 illustrates the results of the numerical simulations. The difference in z magnetization just before readout, ihMTz, is slightly higher for the unsuppressed FSE than the RAGE because of the longer TR, but the use of an inversion preparation to null CSF reduces the ihMT-FLAIR ihMTz to below the RAGE value. This reduction factor is greater for GM than WM because of its longer T1. However, because a much larger flip angle is used for FSE acquisition, the ihMT signal (equal to ihMTz times the sine of the flip angle) is higher for the two FSE acquisitions than for the RAGE.

- **Multiple spin-echoes vs Gradient-echo: image quality**

A representative individual dataset is displayed in Figure 4a, showing the zero-power as well the resulting ihMT. An apparent increase in ihMT SNR can be observed in FSE and FLAIR acquisitions compared to ihMT-RAGE, consistent with theoretical simulations. Consistent with previous observations, we could also observe some ringing in the ihMT-RAGE (27) especially in frontal regions.

Conversely, the use of long refocusing echo-trains in both ihMT-FSE and ihMT-FLAIR led to increased blurring as can be appreciated in Supporting Information Figure S3 when looking at measured PSFs in both phase-encoded directions.

Also noteworthy, when calculating commonly used MTR and ihMTR, we observe division errors in the ihMT-FSE data leading to artificially high ratios as highlighted in Supporting Information Figure S4 because of the sharp CSF-tissue signal intensity

transitions occurring in the M_0 image especially close to the ventricles. Such an issue is eliminated with ihMT-FLAIR. Also, the dark rim at CSF/brain boundaries likely reflects the edge enhanced PSF of CSF after scaling echoes to correct for the T_2 decay of brain tissue.

However, careful examination of image quality does highlight potential for increased ghosting and in-flow artifacts in ihMT-FSE acquisitions especially close to the eyes and in the brainstem (Figure 4b), which appear somewhat reduced or suppressed in the ihMT-FLAIR acquisitions. This CSF artifact in FSE may also lead to more subtle blurring especially in the cortical gray matter due to the presence of pulsating CSF in the subarachnoid space.

The measured 6-min averaged head SAR, while within regulatory limits, was higher in the ihMT-FSE acquisitions (2.62 ± 0.2 W/kg) compared to ihMT-RAGE (1.83 ± 0.14 W/kg) and ihMT-FLAIR (1.82 ± 0.05 W/kg).

- **SNR comparison**

Thermal and physiological noise distributions across the acquisition sequences can be qualitatively assessed by examining Figure 5. Importantly, the tSD spatial distribution seems predominantly dominated by CSF motion in the ihMT-FSE acquisitions, though the effect appears to extend beyond CSF regions with amplitudes significantly higher than in ihMT-RAGE and ihMT-FLAIR. Conversely, both ihMT-RAGE and ihMT-FLAIR have homogeneous tSD distributions. Thermal noise distributions showed lower noise

levels in the ihMT-FSE dataset compared to both ihMT-RAGE and ihMT-FLAIR, with a distribution mimicking a g-factor map because of the use of parallel-imaging reconstruction.

Total SNR maps reflect those observations, showing the spatial dependence in ihMT-FSE with substantial SNR loss in the gray matter compared to ihMT-FLAIR and ihMT-RAGE. It also highlights the overall higher total SNR in ihMT-FLAIR compared to ihMT-RAGE and ihMT-FSE.

Those qualitative observations are confirmed by the quantitative analyses as shown in Figure 6 demonstrating a significantly higher SNR_{rand} in ihMT-FSE acquisitions compared to both ihMT-FLAIR (p=0.005 and p=0.01 for WM and GM) and ihMT-RAGE (p=0.006 and p=0.0002 for WM and GM). However, the SNR_{rand} from ihMT-FLAIR and ihMT-RAGE were not significantly different.

The tSD/rSD ratio was found to be significantly higher in ihMT-FSE compared to both ihMT-FLAIR (p=0.001 and p=0.003 for WM and GM) and ihMT-RAGE (p=0.003 and p=0.004 for WM and GM). ihMT-FLAIR tSD/rSD were found to be significantly lower than ihMT-RAGE ($p=5.10^{-6}$ and p=0.0007 for WM and GM). The highest tSD/rSD ratio was found in the GM with ihMT-FSE.

This leads to total SNR observations, showing that the ihMT-FLAIR SNR_{tot} was significantly higher relative to both ihMT-RAGE (p=0.0006 and p=0.004 for WM and GM, +74% and +49%) and ihMT-FSE (p=0.0001 and $p=7.10^{-6}$ for WM and GM, +187% and +292%). When calculating contrast C, it was found to be higher in ihMT-FLAIR

(0.32 ± 0.03) compared to ihMT-FSE (0.27 ± 0.01, p=0.007) but not significantly different from ihMT-RAGE (0.30 ± 0.02, p=0.43).

- **ihMTsat quantification from different acquisitions**

Group-averaged ihMT differences and ihMTsat maps derived from ihMT-RAGE, ihMT-FSE and ihMT-FLAIR are presented in Figure 7. An apparent increase in WM/GM contrast can be seen in the ihMT-FLAIR difference image in agreement with the simulations that predicted a greater reduction in ihMT difference in gray matter than white matter for ihMT-FLAIR because of its longer T1. With regards to ihMTsat, Although a consistent distribution can be seen through the brain, it is worth noting a substantially higher influence of partial-volume in the ihMTsat derived from ihMT-FLAIR.

The comparison between ihMTsat calculated from ihMT-FSE, ihMT-FLAIR and ihMT-RAGE in Figure 8 shows that while there is a strong correlation in all cases, there was a systematic under-estimation of ihMTsat with FSE acquisitions compared to ihMT-RAGE highlighted in the Bland-Altman plots. In addition, while it was similar for both WM and GM with ihMT-FSE (1.07 vs 1.08), we observed a different slope between WM and GM when comparing ihMT-FLAIR to ihMT-RAGE (0.91 vs 1.13). The highest correlations were found between ihMT-FSE and ihMT-RAGE, with r^2 of 0.86 and 0.93 for GM and WM respectively, while the lowest was found in the GM between ihMT-RAGE and ihMT-FLAIR (r^2=0.73). It is worth noting that the ihMTsat spread, especially in WM ROIs, reflects mostly partial voluming between different brain tissues (WM, GM and CSF).

This overall suggests that ihMTsat is overestimated in the GM and underestimated in the WM in ihMT-FLAIR compared to the ihMT-RAGE likely due to M_0 estimation issues because of CSF/tissue partial-volume as well as added T_1 contrast in ihMT-FLAIR.

- **Spinal cord preliminary application**

Preliminary spinal cord scans showed the feasibility of using ihMT-FLAIR for cervical cord imaging as illustrated in Figure 9. The three datasets collected showed good ihMT signal with some signal decrease in the lower cervical spine consistent with the measured B_1^+ drop (>20% loss below C5).

Discussion

We have successfully implemented an FSE-based sequence for 3D ihMT imaging, which includes an optional dedicated CSF suppression strategy to minimize the impact of physiological noise. Through numerical simulations and *in vivo* qualitative and quantitative comparison, we demonstrated the benefits of FSE over gradient-echo in terms of SNR and overall image quality, while maintaining capabilities for ihMT quantification as illustrated with the modified ihMTsat approach. In addition, we have also highlighted the efficacy of the CSF suppression for reducing physiological noise in 3D FSE for ihMT and explored the feasibility of spinal cord imaging using this approach.

On top of apparent image quality improvement observed at the individual but also group level, the use of long refocusing echo-trains in FSE provided a significant improvement in SNR (defined as the signal over random noise) compared to our gradient-echo based acquisition, even after correcting for T_2-decay related blurring. However, FSE using variably reduced flip-angles (down to a minimum of 50 degrees in our case) comes with an increased sensitivity to physiological motion such as CSF pulsation or eye motion as observed when studying the contribution and relative ratio of physiological and thermal noise. This materializes mainly as phase-ghosting but can also have a subtler global impact on the image and associated quantification as was noted when calculating total SNR. One solution to this problem is the proposed inversion-recovery based CSF suppression strategy (i.e. ihMT-FLAIR) which was shown to be highly efficient in

reducing physiological noise contributions and resulting image degradation, as highlighted through SNR measurements. This came at the cost of reduced temporal efficiency because of long recovery periods. This also led to an increased apparent WM/GM contrast in the ihMT-FLAIR difference images, resulting from a mixed T_1 and ihMT contrast that is predicted by our simulations. But the modified ihMTsat method allowed disentangling this as demonstrated by the good agreement in both white and gray matter regions between ihMTsat calculated with ihMT-RAGE and ihMT-FLAIR. More generally, this study shows that the ihMTsat framework allows quantitative ihMT with various imaging sequences.

In addition, while gradient-echo has been successfully used for spinal cord ihMT acquisitions (27,29,47), preliminary results have shown the feasibility of ihMT-FLAIR for spinal cord imaging combining centric-out k-space view-ordering and interleaved saturation schemes. As for brain acquisitions, optimizing VFA design, k-space sampling and reconstruction could certainly address potential contrast degradation due to T_2-blurring. The impact of cardiac cycle related CSF motion should also be investigated (25) as well as potential B_0/B_1 issues that could have led to reduced ihMT signal in the lower spinal cord and variable background signal.

It is worth mentioning that while the estimated SAR in the ihMT-FSE acquisitions was higher than the ihMT-RAGE with a similar ihMT preparation (+43%), the power deposition remained within regulatory limits. ihMT-FLAIR was not associated with a substantial higher power deposition because of the use of a long TR for sufficient signal recovery.

Some limitations of our study have to be considered. Indeed, while we assumed a perfect inversion for CSF suppression, partial loss of efficiency or partial saturation of the bound pool may lead to quantification inaccuracies. However, C-shaped FOCI pulses are known for extremely high inversion efficiency (>99%) most likely minimizing the potential effect of efficiency (33).

Our results also failed to realize the full SNR gain predicted by theory. While simulations showed a range of increase between 1.9 with the implemented ihMT-FLAIR to 6.5-fold with ihMT-FSE, a more modest yet significant SNR_{rand} (which corresponds to the ihMT signal simulated) increase was measured. Considering transverse relaxation in the simulations could explain at least a fraction of this mismatch. Moreover, simulations did not consider physiological noise which has been shown to be the most significant contributor in this study. Additionally, the different acquisition order (interleaved vs. sequential) could have potentially impacted the retrospective motion-correction strategy.

When considering quantification, commonly used ihMTR calculation can be problematic close to CSF regions (e.g. close to the ventricles or cortical gray matter) because of the partial volume effects or nulled CSF signal which would require correction strategies.

As seen when comparing the ihMTsat data from the different acquisitions, although in generally good agreement, there was a systematic bias in the ihMT-FSE and ihMT-FLAIR derived ihMTsat maps compared to ihMT-RAGE, more pronounced in the ihMT-FLAIR warranting further investigation. The systematic underestimation of ihMTsat with ihMT-FSE compared to ihMT-RAGE could also be explained by the different saturation ordering scheme (interleaved vs sequential) as described previously by Varma et al (27). It is also worth noting that the MP2RAGE derived T_1 maps are not perfectly

immune to the effect of transmit (B_1^+) inhomogeneities, potentially leading to additional uncertainties in the ihMTsat quantification.

Several improvements to the FSE acquisition sequence could further increase its appeal. First, the sequence may be further accelerated using pseudo random undersampling of k-space combined with Compressed Sensing reconstruction. Also, further optimization of the variable flip-angle echo train could provide a better balance between T_2-blurring, motion-sensitivity and power deposition (39). To overcome the time penalty imposed by the long recovery required for ihMT-FLAIR, alternative strategies for CSF suppression could be envisioned such as a T_2-FLAIR preparation (48). Finally, potential strategies for deriving M_0 using a homogenous reference for example could be explored (49) to tackle the issue arising from sharp intensity transitions at the edges between brain tissue and CSF coming from the FSE point-spread function.

Finally, this work, complementary to previous literature on CEST (8) or ASL (7,50), further confirms the potential of 3D FSE for magnetization-prepared contrasts. It also shows that targeted signal suppression strategies can be implemented when needed and accounted for in quantification as highlighted by our use of ihMTsat. While the historically long acquisition times, lower temporal efficiency and high power deposition of FSE sequence have led to favoring gradient-echo based sequences for 3D magnetization-prepared contrasts, this growing body of work shows that 3D FSE can be a robust and sensitive sequence not only for qualitative anatomical imaging but also quantitative microstructural and functional imaging.

Conclusions

In conclusion, we have proposed the use of 3D multiple spin echoes for acquisition of magnetization prepared ihMT imaging. We highlighted the benefits but also the challenges of FSE imaging for this purpose and showed the potential benefits of a dedicated CSF-suppression strategy to tackle FSE issues. Altogether, we have demonstrated the potential for high quality and quantitative brain imaging using 3D FSE readout. This work contributes to a growing literature showing 3D FSE can be a high SNR acquisition approach with reasonable scan times for magnetization prepared contrasts that can compete with more time-efficient but lower SNR gradient-echo based sequences.

Data availability statement

The code used for simulations is derived from the repository available at https://github.com/gvarma617/ihMTRAGE-optimize. For the pseudo-replica, we used the code provided at http://hansenms.github.io/sunrise/sunrise2013/.

Acknowledgments

The authors gratefully acknowledge Fotini Papadopoulou RT(MR), Stephanie Waldman BA, Lauren Phung BS and Nancy Otaluka BA for their support in conducting this study.

Disclosures

David C. Alsop is an inventor on patents related to the pseudo-continuous ASL method not used in the current work. He receives post-market royalties through his institution from GE Healthcare, Siemens Healthineers, Philips Healthcare, Hitachi Medical and Animage LLC. He additionally receives research support from GE Healthcare.

References

1. Mugler III JP, Brookeman JR. Rapid three-dimensional T1-weighted MR imaging with the MP-RAGE sequence. Journal of Magnetic Resonance Imaging 1991;1:561–567 doi: 10.1002/jmri.1880010509.
2. Mugler JP, Bao S, Mulkern RV, et al. Optimized Single-Slab Three-dimensional Spin-Echo MR Imaging of the Brain. Radiology 2000;216:891–899 doi: 10.1148/radiology.216.3.r00au46891.
3. Busse RF, Hariharan H, Vu A, Brittain JH. Fast spin echo sequences with very long echo trains: Design of variable refocusing flip angle schedules and generation of clinical T2 contrast. Magnetic Resonance in Medicine 2006;55:1030–1037 doi: 10.1002/mrm.20863.
4. Mugler III JP, Bao S, Mulkern RV, Guttmann CR, Jolesz FA, Brookeman JR. Three-dimensional Spin-Echo-Train Proton-Density-Weighted Imaging using Shaped Signal Evolutions. In: Proceedings of the 7th annual meeting of the ISMRM. Philadelphia, PA; 1999. p. 1631.
5. Schaffter T, Bornert P, Leibfritz D. PSF improvements in single shot GRASE imaging. In: Proceedings of the 2nd annual meeting of the Society for Magnetic Resonance (SMR). San Francisco, CA; 1994. p. 27.
6. Mugler JP. Optimized three-dimensional fast-spin-echo MRI. Journal of Magnetic Resonance Imaging 2014;39:745–767 doi: 10.1002/jmri.24542.
7. Taso M, Zhao L, Guidon A, Litwiller DV, Alsop DC. Volumetric abdominal perfusion measurement using a pseudo-randomly sampled 3D fast-spin-echo (FSE) arterial spin labeling (ASL) sequence and compressed sensing reconstruction. Magnetic Resonance in Medicine 2019;82:680–692 doi: 10.1002/mrm.27761.
8. Zhang Y, Yong X, Liu R, et al. Whole-brain chemical exchange saturation transfer imaging with optimized turbo spin echo readout. Magnetic Resonance in Medicine 2020;84:1161–1172 doi: 10.1002/mrm.28184.
9. Varma G, Duhamel G, de Bazelaire C, Alsop DC. Magnetization transfer from inhomogeneously broadened lines: A potential marker for myelin. Magnetic Resonance in Medicine 2015;73:614–22 doi: 10.1002/mrm.25174.
10. Duhamel G, Prevost VH, Cayre M, et al. Validating the sensitivity of inhomogeneous magnetization transfer (ihMT) MRI to myelin with fluorescence microscopy. NeuroImage 2019;199:289–303 doi: 10.1016/j.neuroimage.2019.05.061.
11. Varma G, Girard OM, Prevost VH, Grant AK, Duhamel G, Alsop DC. In vivo measurement of a new source of contrast, the dipolar relaxation time, T1D, using a modified inhomogeneous magnetization transfer (ihMT) sequence. Magnetic Resonance in Medicine 2017;78:1362–1372 doi: 10.1002/mrm.26523.
12. Carvalho VND, Hertanu A, Grélard A, et al. MRI assessment of multiple dipolar relaxation time (T1D) components in biological tissues interpreted with a generalized inhomogeneous magnetization transfer (ihMT) model. Journal of Magnetic Resonance 2020;311:106668 doi: 10.1016/j.jmr.2019.106668.
13. Swanson SD, Malyarenko DI, Fabiilli ML, Welsh RC, Nielsen J-F, Srinivasan A. Molecular, dynamic, and structural origin of inhomogeneous magnetization transfer in

lipid membranes. Magnetic Resonance in Medicine 2017;77:1318–1328 doi: 10.1002/mrm.26210.
14. Varma G, Girard OM, Prevost VH, Grant AK, Duhamel G, Alsop DC. Interpretation of magnetization transfer from inhomogeneously broadened lines (ihMT) in tissues as a dipolar order effect within motion restricted molecules. Journal of Magnetic Resonance 2015;260:67–76 doi: 10.1016/j.jmr.2015.08.024.
15. Manning AP, Chang KL, MacKay AL, Michal CA. The physical mechanism of "inhomogeneous" magnetization transfer MRI. Journal of Magnetic Resonance 2017;274:125–136 doi: 10.1016/j.jmr.2016.11.013.
16. Taso M, Girard OM, Duhamel G, et al. Tract-specific and age-related variations of the spinal cord microstructure: a multi-parametric MRI study using diffusion tensor imaging (DTI) and inhomogeneous magnetization transfer (ihMT). NMR Biomed 2016;29:817–832 doi: 10.1002/nbm.3530.
17. Geeraert BL, Lebel RM, Mah AC, et al. A comparison of inhomogeneous magnetization transfer, myelin volume fraction, and diffusion tensor imaging measures in healthy children. NeuroImage 2017 doi: 10.1016/j.neuroimage.2017.09.019.
18. Ercan E, Varma G, Mädler B, et al. Microstructural correlates of 3D steady-state inhomogeneous magnetization transfer (ihMT) in the human brain white matter assessed by myelin water imaging and diffusion tensor imaging. Magnetic Resonance in Medicine 2018;80:2402–2414 doi: 10.1002/mrm.27211.
19. Munsch F, Varma G, Taso M, et al. Characterization of the cortical myeloarchitecture with inhomogeneous magnetization transfer imaging (ihMT). NeuroImage 2021;225:117442 doi: 10.1016/j.neuroimage.2020.117442.
20. Rasoanandrianina H, Demortière S, Trabelsi A, et al. Sensitivity of the Inhomogeneous Magnetization Transfer Imaging Technique to Spinal Cord Damage in Multiple Sclerosis. American Journal of Neuroradiology 2020;41:929–937 doi: 10.3174/ajnr.A6554.
21. Rasoanandrianina Henitsoa, Grapperon Aude-Marie, Taso Manuel, et al. Region-specific impairment of the cervical spinal cord (SC) in amyotrophic lateral sclerosis: A preliminary study using SC templates and quantitative MRI (diffusion tensor imaging/inhomogeneous magnetization transfer). NMR in Biomedicine 2017;30:e3801 doi: 10.1002/nbm.3801.
22. Van Obberghen E, Mchinda S, le Troter A, et al. Evaluation of the Sensitivity of Inhomogeneous Magnetization Transfer (ihMT) MRI for Multiple Sclerosis. AJNR Am J Neuroradiol 2018;39:634–641 doi: 10.3174/ajnr.A5563.
23. Varma G, Girard OM, Mchinda S, et al. Low duty-cycle pulsed irradiation reduces magnetization transfer and increases the inhomogeneous magnetization transfer effect. Journal of Magnetic Resonance 2018;296:60–71 doi: 10.1016/j.jmr.2018.08.004.
24. Girard OM, Prevost VH, Varma G, Cozzone PJ, Alsop DC, Duhamel G. Magnetization transfer from inhomogeneously broadened lines (ihMT): Experimental optimization of saturation parameters for human brain imaging at 1.5 Tesla. Magnetic Resonance in Medicine 2015;73:2111–2121 doi: 10.1002/mrm.25330.
25. Girard OM, Callot V, Prevost VH, et al. Magnetization transfer from inhomogeneously broadened lines (ihMT): Improved imaging strategy for spinal cord applications. Magnetic Resonance in Medicine 2017;77:581–591 doi: 10.1002/mrm.26134.

26. Malik SJ, Teixeira RPAG, West DJ, Wood TC, Hajnal JV. Steady-state imaging with inhomogeneous magnetization transfer contrast using multiband radiofrequency pulses. Magnetic Resonance in Medicine 2020;83:935–949 doi: https://doi.org/10.1002/mrm.27984.
27. Varma G, Munsch F, Burns B, et al. Three-dimensional inhomogeneous magnetization transfer with rapid gradient-echo (3D ihMTRAGE) imaging. Magnetic Resonance in Medicine 2020;84:2964–2980 doi: https://doi.org/10.1002/mrm.28324.
28. Mchinda S, Varma G, Prevost VH, et al. Whole brain inhomogeneous magnetization transfer (ihMT) imaging: Sensitivity enhancement within a steady-state gradient echo sequence. Magnetic Resonance in Medicine 2018;79:2607–2619 doi: 10.1002/mrm.26907.
29. Ercan E, Varma G, Dimitrov IE, et al. Combining inhomogeneous magnetization transfer and multipoint Dixon acquisition: Potential utility and evaluation. Magnetic Resonance in Medicine 2021;85:2136–2144 doi: 10.1002/mrm.28571.
30. Wood TC, Damestani NL, Lawrence AJ, et al. Silent myelin-weighted magnetic resonance imaging. Wellcome Open Res 2020;5 doi: 10.12688/wellcomeopenres.15845.2.
31. Taso M, Munsch F, Guidon A, et al. Variable-density Fast-Spin-Echo (FSE) for volumetric inhomogeneous Magnetization Transfer (ihMT) imaging. In: Proceedings of the 28th annual meeting of the ISMRM. Virtual; 2020. p. 3140.
32. Helms G, Dathe H, Kallenberg K, Dechent P. High-resolution maps of magnetization transfer with inherent correction for RF inhomogeneity and T1 relaxation obtained from 3D FLASH MRI. Magnetic Resonance in Medicine 2008;60:1396–1407 doi: 10.1002/mrm.21732.
33. Ordidge RJ, Wylezinska M, Hugg JW, Butterworth E, Franconi F. Frequency offset corrected inversion (FOCI) pulses for use in localized spectroscopy. Magn. Reson. Med. 1996;36:562–566 doi: 10.1002/mrm.1910360410.
34. Varma G, Girard OM, Prevost VH, Grant AK, Duhamel G, Alsop DC. Interpretation of magnetization transfer from inhomogeneously broadened lines (ihMT) in tissues as a dipolar order effect within motion restricted molecules. Journal of magnetic resonance 2015;260:67–76 doi: 10.1016/j.jmr.2015.08.024.
35. Stanisz GJ, Odrobina EE, Pun J, et al. T1, T2 relaxation and magnetization transfer in tissue at 3T. Magnetic Resonance in Medicine 2005;54:507–512 doi: 10.1002/mrm.20605.
36. Marques JP, Kober T, Krueger G, van der Zwaag W, Van de Moortele P-F, Gruetter R. MP2RAGE, a self bias-field corrected sequence for improved segmentation and T1-mapping at high field. NeuroImage 2010;49:1271–1281 doi: 10.1016/j.neuroimage.2009.10.002.
37. McKenzie CA, Yeh EN, Ohliger MA, Price MD, Sodickson DK. Self-calibrating parallel imaging with automatic coil sensitivity extraction. Magnetic Resonance in Medicine 2002;47:529–538 doi: 10.1002/mrm.10087.
38. Uecker, M., Tamir, J., Bahri, D., et al. Berkeley Advanced Reconstruction Toolbox. In: Proc. Intl. Soc. Mag. Reson. Med. Toronto, ON, Canada; 2015. p. 2486.
39. Zhao L, Chang C-D, Alsop DC. Controlling T2 blurring in 3D RARE arterial spin labeling acquisition through optimal combination of variable flip angles and k-space filtering. Magnetic Resonance in Medicine 2018;80:1391–1401 doi:

10.1002/mrm.27118.
40. Weigel M. Extended phase graphs: Dephasing, RF pulses, and echoes - pure and simple. Journal of Magnetic Resonance Imaging 2015;41:266–295 doi: 10.1002/jmri.24619.
41. Krist JE. Deconvolution of Hubble Space Telescope Images using Simulated Point Spread Functions. 1992;25:226.
42. Biggs DSC, Andrews M. Acceleration of iterative image restoration algorithms. Appl. Opt., AO 1997;36:1766–1775 doi: 10.1364/AO.36.001766.
43. Avants BB, Tustison NJ, Song G, Cook PA, Klein A, Gee JC. A Reproducible Evaluation of ANTs Similarity Metric Performance in Brain Image Registration. Neuroimage 2011;54:2033–2044 doi: 10.1016/j.neuroimage.2010.09.025.
44. Robson PM, Grant AK, Madhuranthakam AJ, Lattanzi R, Sodickson DK, McKenzie CA. Comprehensive quantification of signal-to-noise ratio and g-factor for image-based and k-space-based parallel imaging reconstructions. Magnetic Resonance in Medicine 2008;60:895–907 doi: 10.1002/mrm.21728.
45. Alsop DC, Munsch F, Varma G, Duhamel G. Quantification of Magnetization Transfer and Inhomogeneous Magnetization Transfer with an MPRAGE sequence and an MTsat Approach. In: Proceedings of the 28th annual meeting of the ISMRM. ; 2020. p. 3142.
46. De Leener B, Lévy S, Dupont SM, et al. SCT: Spinal Cord Toolbox, an open-source software for processing spinal cord MRI data. NeuroImage 2017;145:24–43 doi: 10.1016/j.neuroimage.2016.10.009.
47. Troalen T, Callot V, Varma G, et al. Cervical Spine inhomogeneous Magnetization Transfer (ihMT) Imaging Using ECG-Triggered 3D Rapid Acquisition Gradient-Echo (ihMT-RAGE). In: Proceedings of the 27th annual meeting of the ISMRM. Montreal, QC, Canada; 2019. p. 300.
48. Wong EC, Liu TT, Luh W-M, Frank LR, Buxton RB. T1 and T2 selective method for improved SNR in CSF-attenuated imaging: T2-FLAIR. Magnetic Resonance in Medicine 2001;45:529–532 doi: 10.1002/1522-2594(200103)45:3<529::AID-MRM1071>3.0.CO;2-L.
49. Dai W, Robson PM, Shankaranarayanan A, Alsop DC. Sensitivity calibration with a uniform magnetization image to improve arterial spin labeling perfusion quantification. Magnetic Resonance in Medicine 2011;66:1590–1600 doi: 10.1002/mrm.22954.
50. Taso M, Munsch F, Zhao L, Alsop DC. Regional and depth-dependence of cortical blood-flow assessed with high-resolution Arterial Spin Labeling (ASL). J Cereb Blood Flow Metab 2021:0271678X20982382 doi: 10.1177/0271678X20982382.

Appendix: model equations for MTsat quantification of FSE data

Similar to the Appendix of Munsch et al, where the equations for MTsat quantification of MPRAGE data are described, we modeled the effect of each MT pulse as an attenuation of free pool magnetization by a factor of (1 - δ), where δ is the MTsat factor for that pulse. Our FSE acquisition differs from the MPRAGE in two ways. One is that the larger refocusing pulses, combined with a post-acquisition saturation, eliminate longitudinal magnetization after the acquisition. The other is the inclusion of an optional inversion recovery pulse for CSF suppression. The calculation was performed by stepping across multiple time periods: the wait between the (optional) non-selective inversion and the MT preparation (T_{wait}), the preparation time (T_{ihMT}=n*ihMT$_{TR}$), the delay before acquisition (w_d), and the recovery after acquisition + post-readout saturation time (T_{read}).

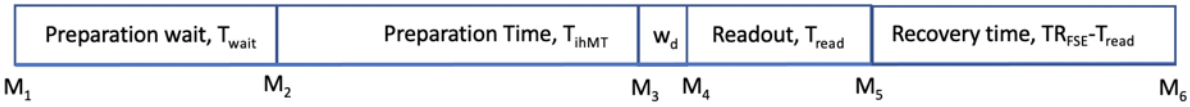

$$M_2 = \pm M_1 e^{-\frac{T_{wait}}{T_1}} + M_0\left(1 - e^{-\frac{T_{wait}}{T_1}}\right)$$

$$M_3 = M_2(1-\delta)^n e^{-\frac{T_{ihMT}}{T_1}} + M_0(1 - e^{-\frac{ihMT_{TR}}{T_1}})\frac{(1-(1-\delta)^n e^{-\frac{T_{ihMT}}{T_1}})}{(1-(1-\delta)e^{-\frac{ihMT_{TR}}{T_1}})}$$

$$M_4 = M_3 e^{-\frac{w_d}{T_1}} + M_0(1 - e^{-\frac{w_d}{T_1}})$$

$$M_5 = 0$$

$$M_6 = M_0\left(1 - e^{-\frac{TR_{FSE}-T_{read}}{T_1}}\right)$$

$$M_{1'} = M_6$$

Where T_{read} is the sum of the readout and post-readout saturation duration times. For reasonable parameters, the ratio of the MT image to the zero-power reference image is a monotonic function of δ. These can readily be solved for each pixel of the volume by a robust bisection method.

In addition, the zero-power reference image was scaled to estimate true M_0 accounting for signal attenuation because of TR/TI by the following:

$$S = 1 - 2e^{-\frac{TI}{T_1}} + e^{-\frac{(TR_{FSE} - T_{read})}{T_1}}$$

Tables

	ihMT-RAGE	ihMT-FSE	ihMT-FLAIR
Image orientation	Sagittal	Sagittal	Sagittal
Number of slices	64	64	64
Resolution (mm^3)	2.4 x 2.4 x 2.8	2.4 x 2.4 x 2.8	2.4 x 2.4 x 2.8
$B_{1,ihMT}$ (uT)	12	12	12
$ihMT_{TR}$ (ms)	100	100	100
T_{ihMT} (ms)	900	900	900
TR (ms)	2000	4000	6000
TE (ms)	1.3	15.5	15.5
TI (ms)	N/A	N/A	2000
Flip-angle (deg)	10	90 - VFA	90 - VFA
Receiver bandwidth (kHz)	35.6	31.25	31.25
Number of averages	2	2	1
Views per segment / ETL	90	130	130
Echo spacing	3.6	3.1	3.1

View-ordering	Radial fan-beam	Radial fan-beam	Radial fan-beam
Post-readout saturation	No	Yes	Yes
Saturation ordering	Sequential	Interleaved	Interleaved
Acquisition time (min)	7 min 20	10 min	7 min 30

Table 1 - Imaging parameters

Figures captions

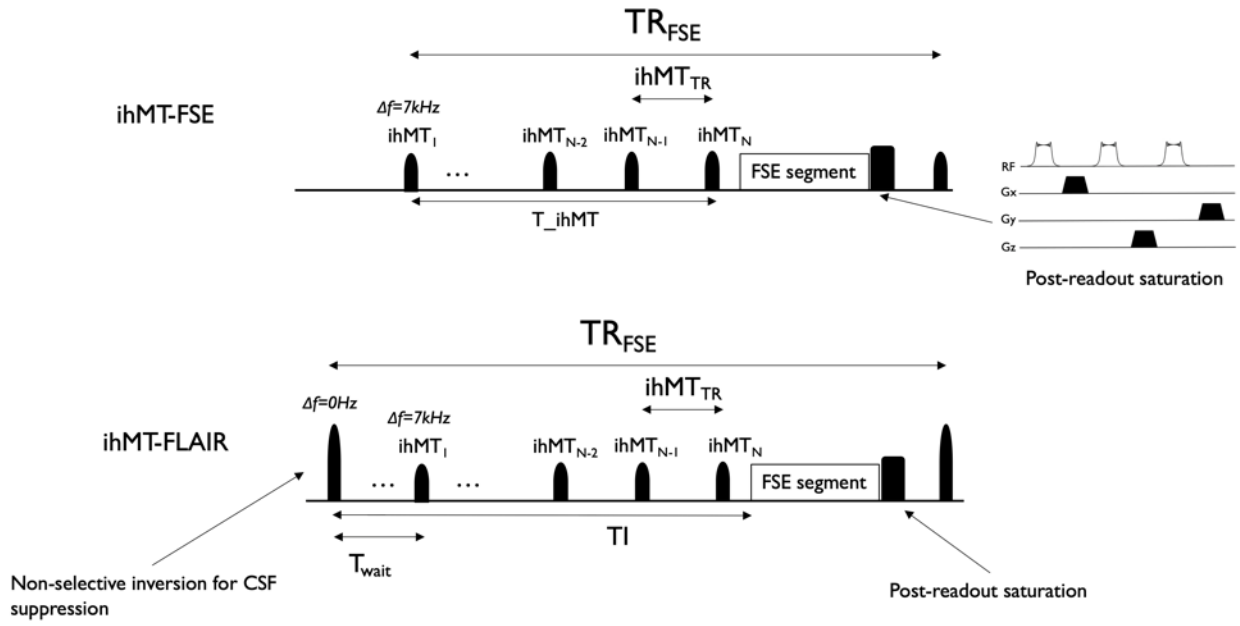

Figure 1 - ihMT-FSE and ihMT-FLAIR sequence diagrams

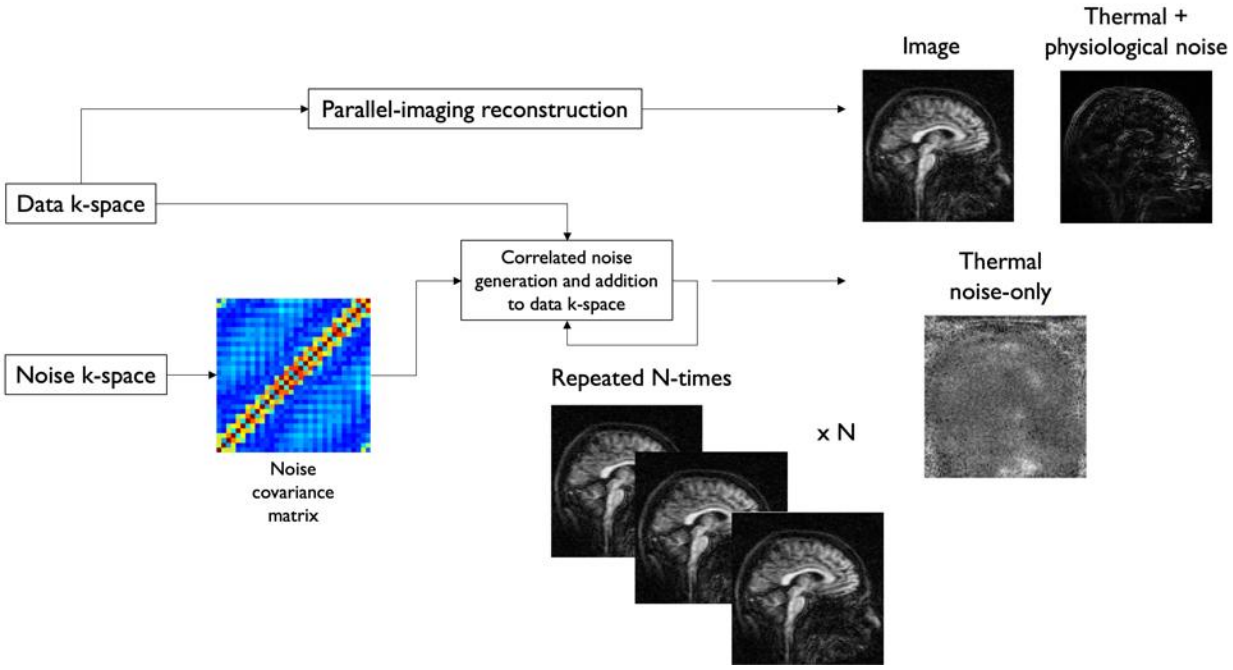

Figure 2 - SNR and physiological noise measurement pipeline

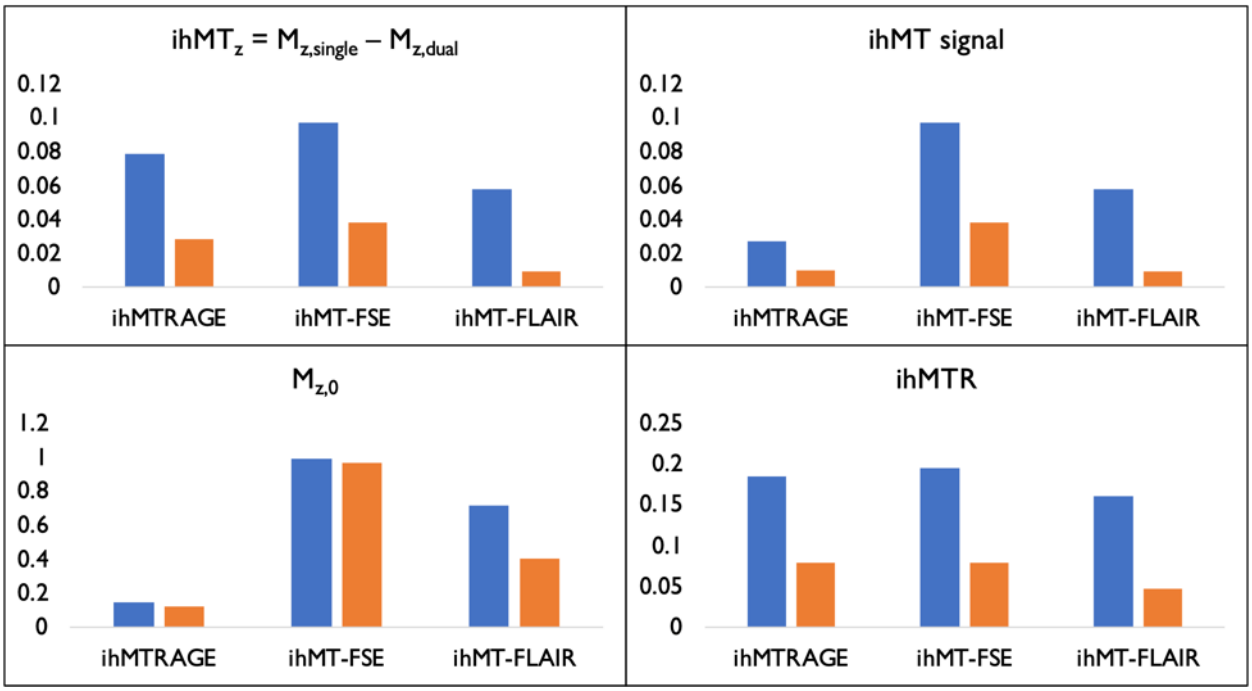

Figure 3 - Results of numerical simulations showing the difference in longitudinal magnetization between single ($M_{z,single}$) and dual-frequency saturation ($M_{z,dual}$) ($ihMT_z$), ihMT signal after initial excitation (ihMT signal), zero power longitudinal magnetization $M_{z,0}$, ihMTR.

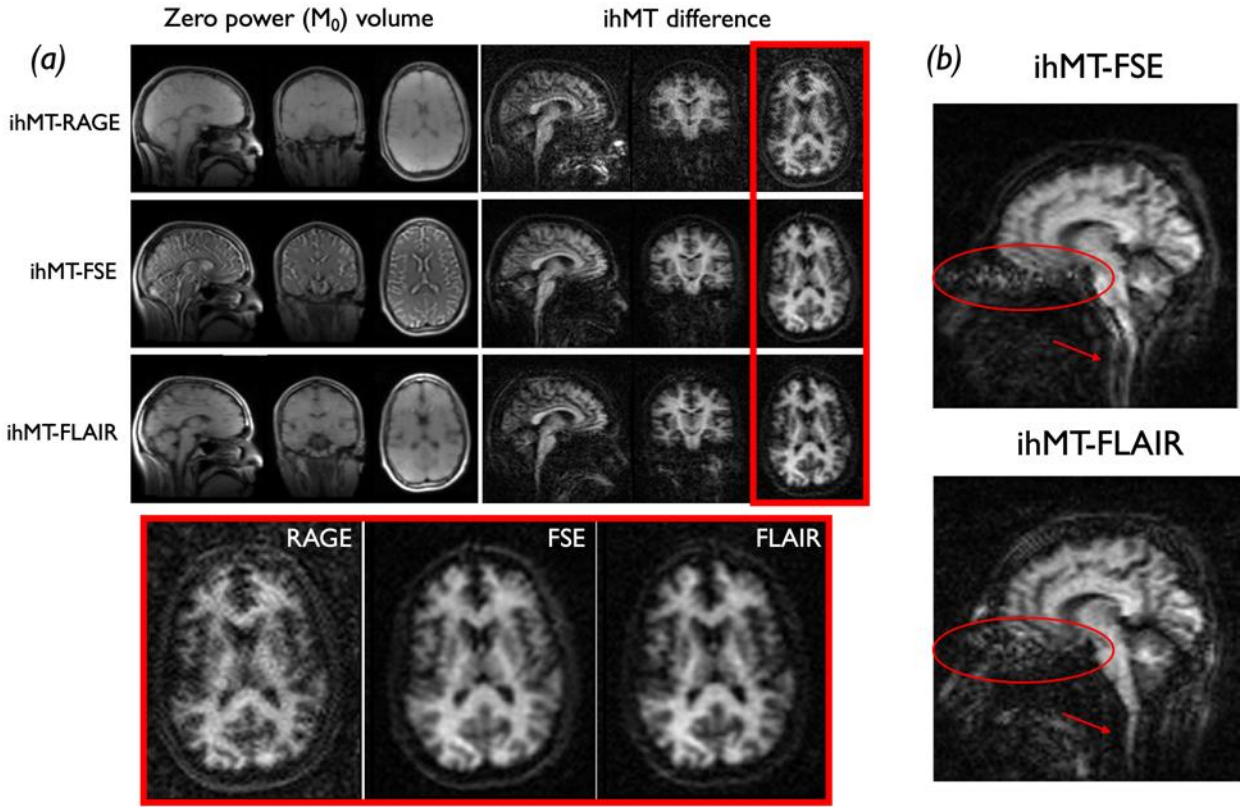

Figure 4 - (a) M_0 and ihMT difference images acquired with ihMT-RAGE, ihMT-FSE and ihMT-FLAIR in a representative subject. Edge enhancement in the M_0 FSE image, and potentially apparent blurring of CSF boundaries in M_0 FLAIR images reflects the different point spread function of long T_2 CSF compared to gray and white matter. For illustration purposes, the ihMT difference images were scaled by normalizing each by their mean value. (b) illustration of CSF-motion related artifacts in ihMT-FSE compared to ihMT-FLAIR. Red arrows/circle show areas with increased ghosting artifacts in the FSE compared to FLAIR

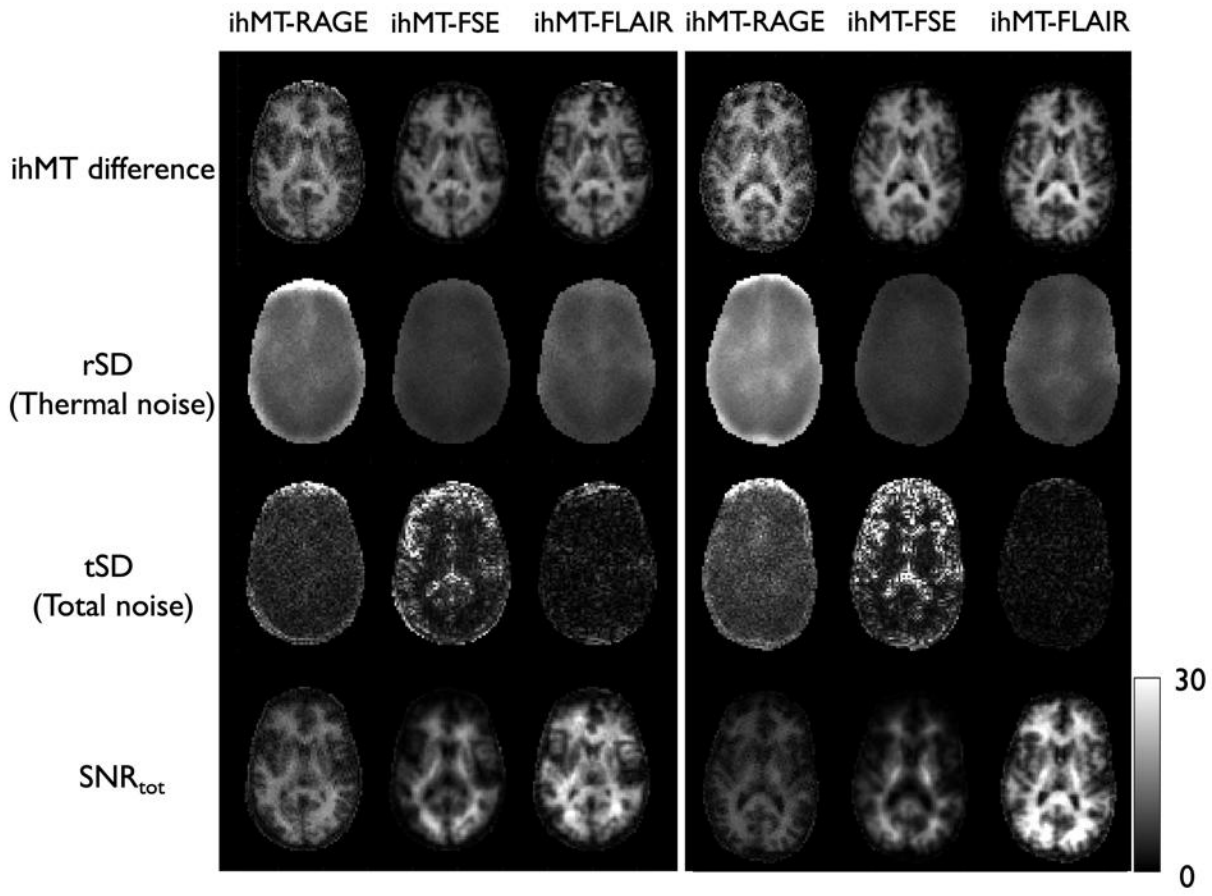

Figure 5 - ihMT difference image, random noise-only image (rSD), temporal standard-deviation (tSD) image reflecting physiological and thermal noise and total SNR (SNR_{tot}) maps in two volunteers. IhMT differences, rSD and tSD were normalized by their respective M_0 image (after smoothing) to provide a comparable scale and windowed to highlight their spatial distribution

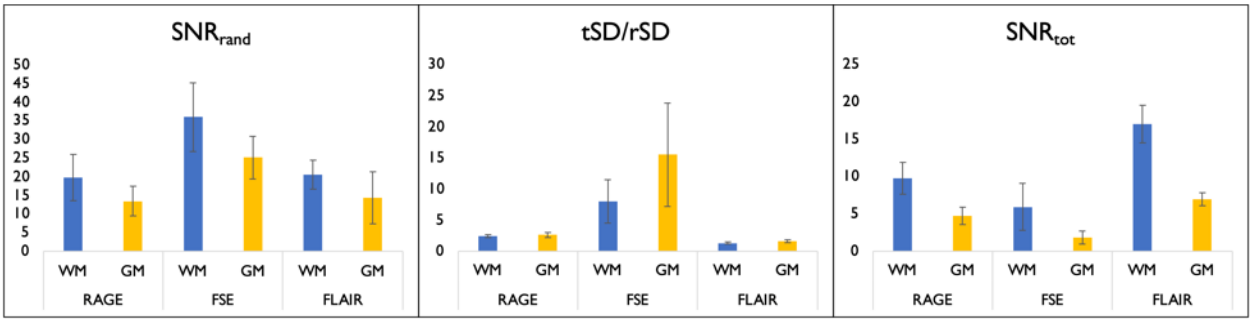

Figure 6 – thermal SNR (SNR_{rand}), ratio of total/random noise (tSD/rSD) and total SNR (SNR_{tot}) bar charts

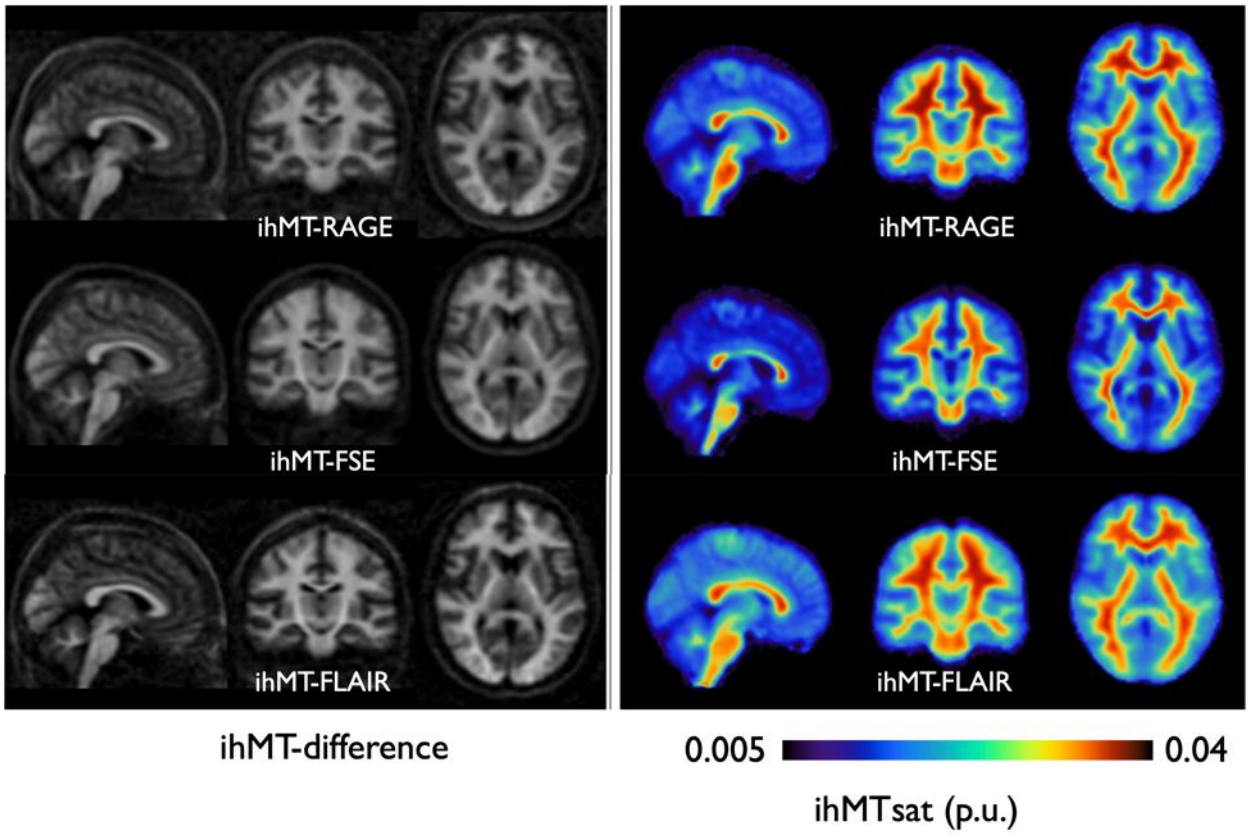

Figure 7 - N=5 group-averaged ihMT difference and ihMTsat maps for ihMT-RAGE (top), ihMT-FSE (middle) and ihMT-FLAIR (bottom)

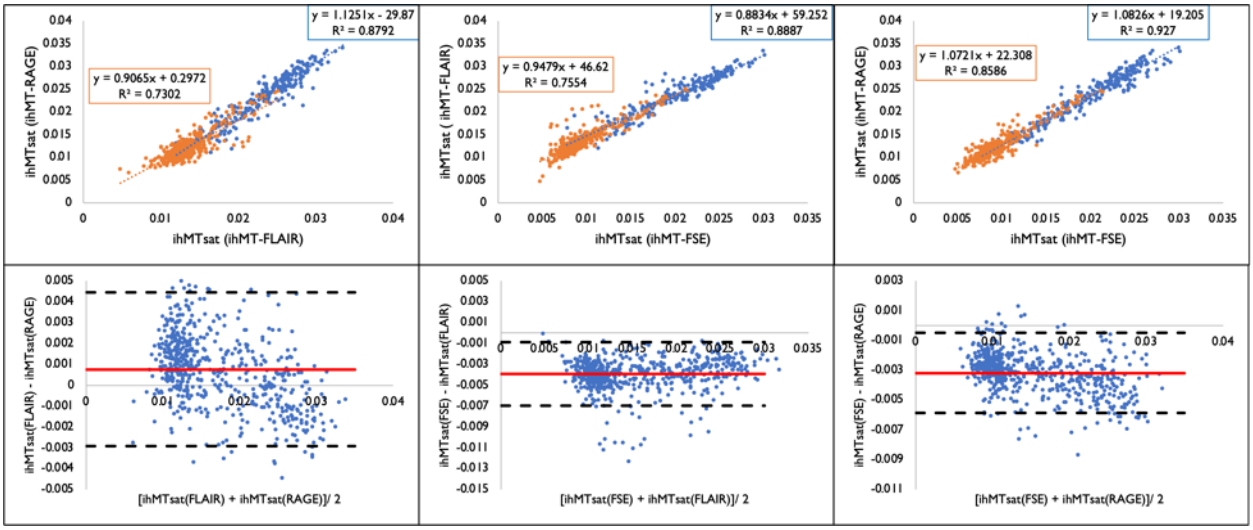

Figure 8 - Scatter-plots and associated Bland-Altman plots comparing ihMTsat quantification between different acquisitions. In all scatter plots, a linear fit for the GM (orange) and WM (blue) was performed and the equation and determination coefficient are displayed.

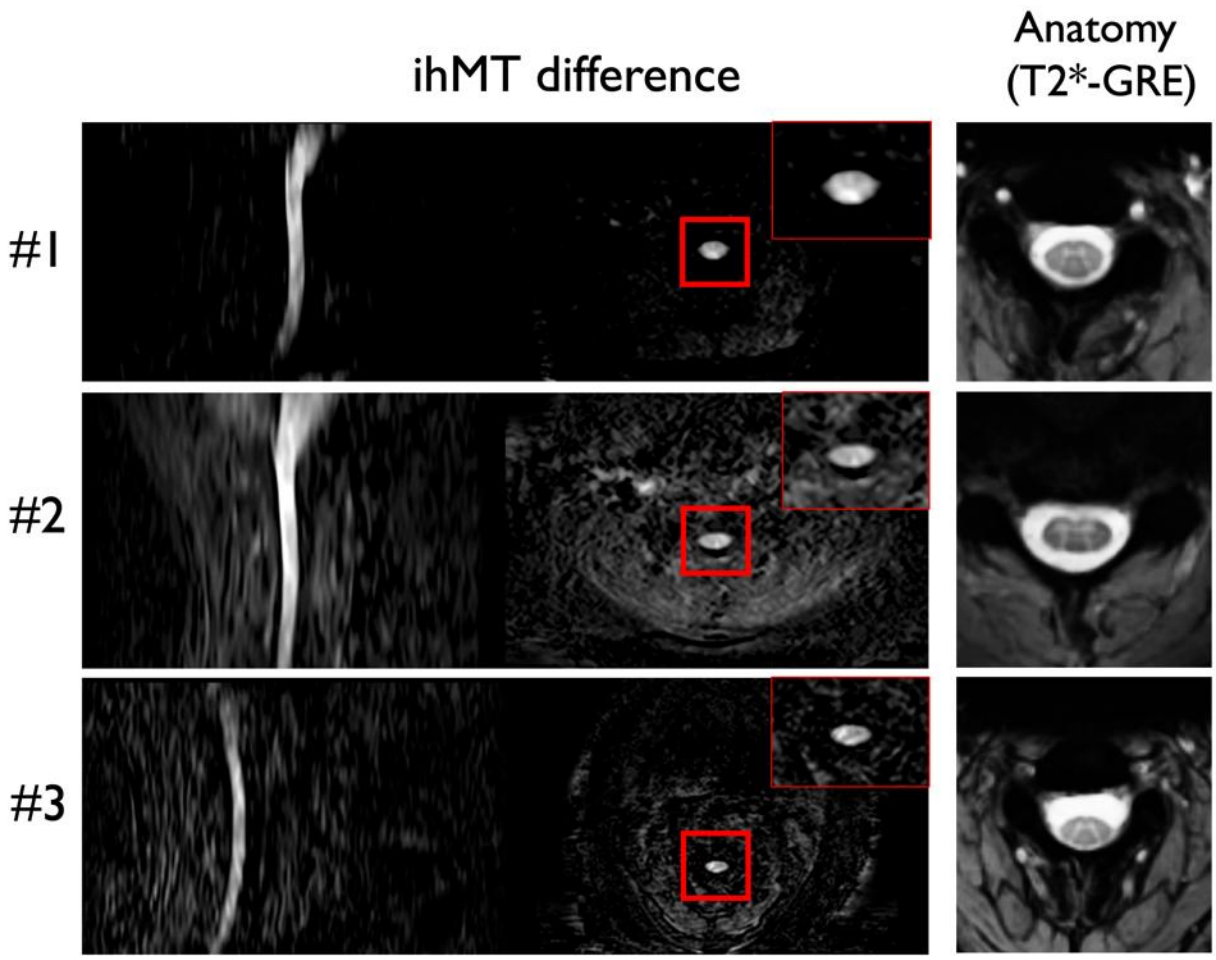

Figure 9 - Preliminary spinal cord ihMT-FLAIR difference volumes in three healthy volunteers as well as T_2*-weighted multi-echo GRE for anatomical comparison

Supporting Information

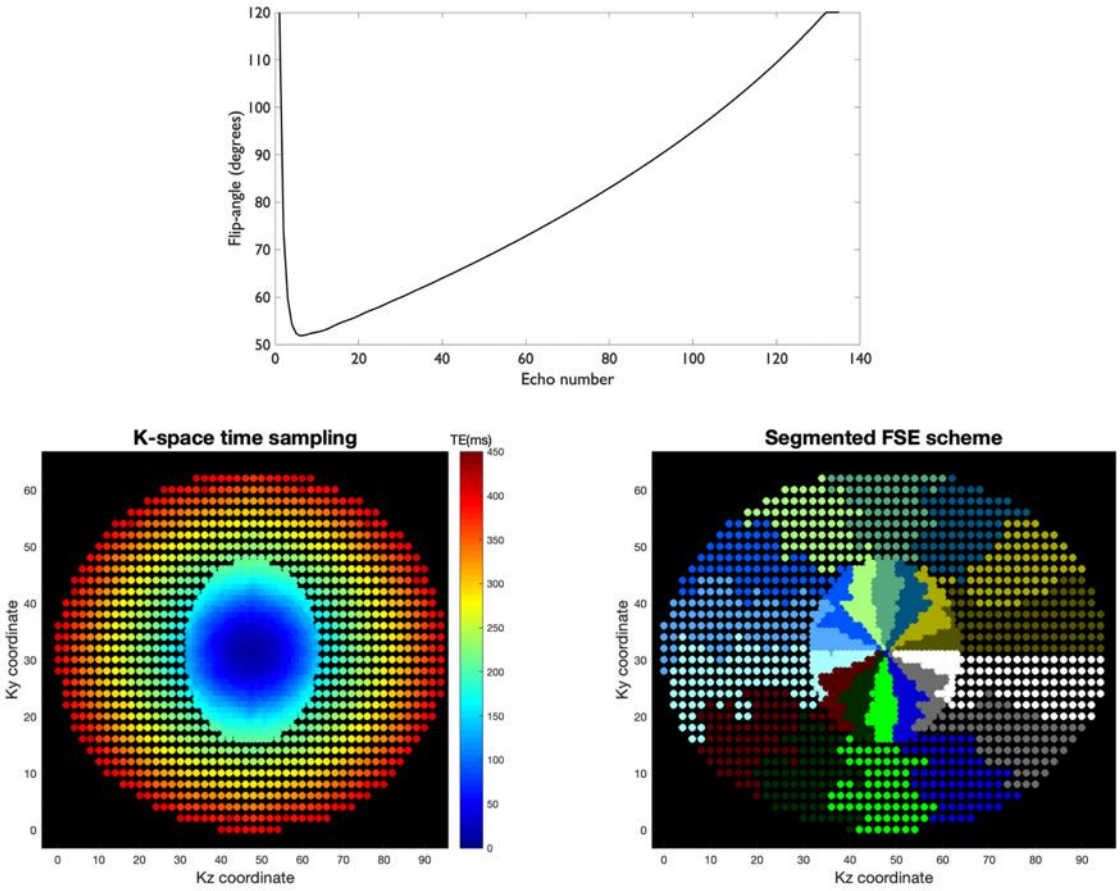

Supporting Information Figure S1: Top – variable flip-angle echo train, Bottom left – k-space time-sampling and Bottom right – segmented FSE scheme

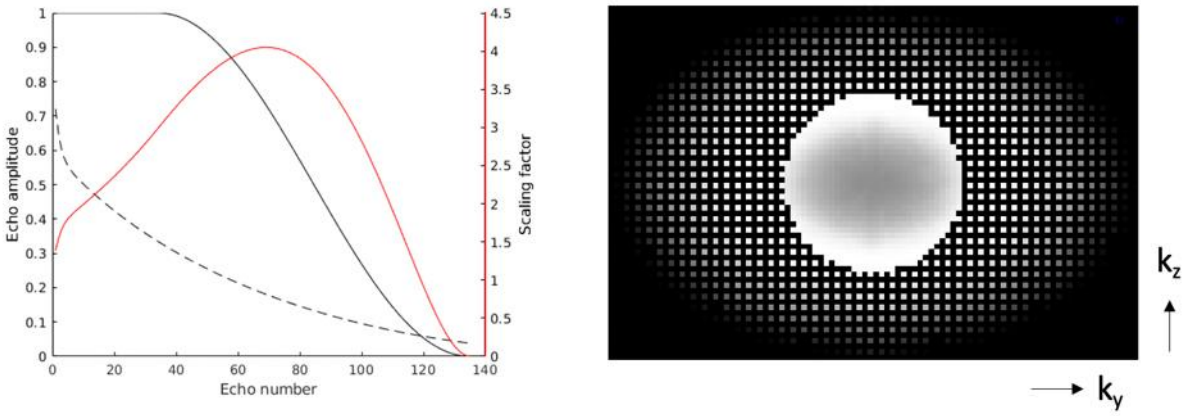

Supporting Information Figure S2 - Illustration of the echo train scaling procedure showing the simulated (dashed black line) echo amplitude across the echo-train for intermediate T1/T2 = 1250/80ms between white and gray matter, the target Tukey window (full black line) and the echo scaling factor (secondary axis, red) and k-space filter

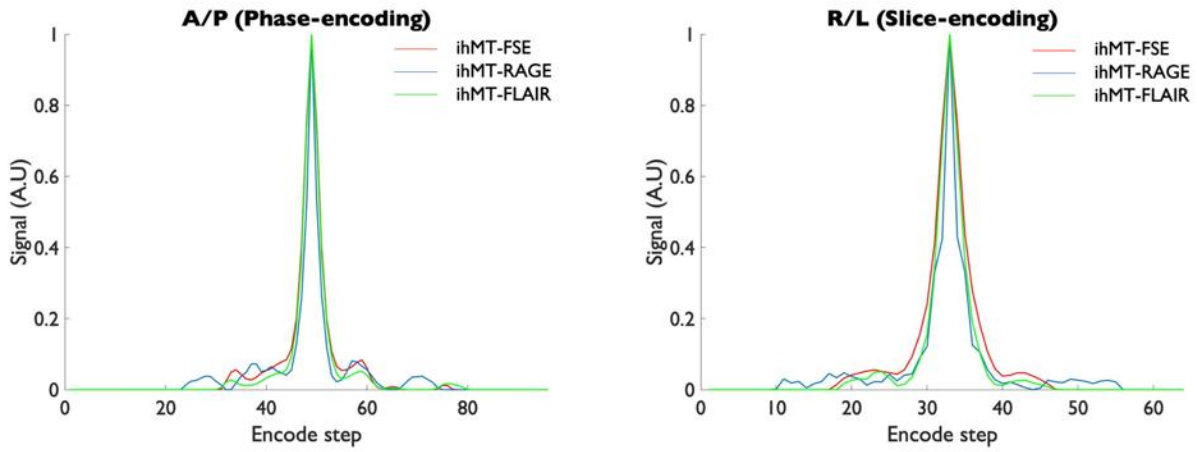

Supporting Information Figure S3: Measured Point-Spread Function using a blind deconvolution method in both phase and slice-encoding directions for all three sequences

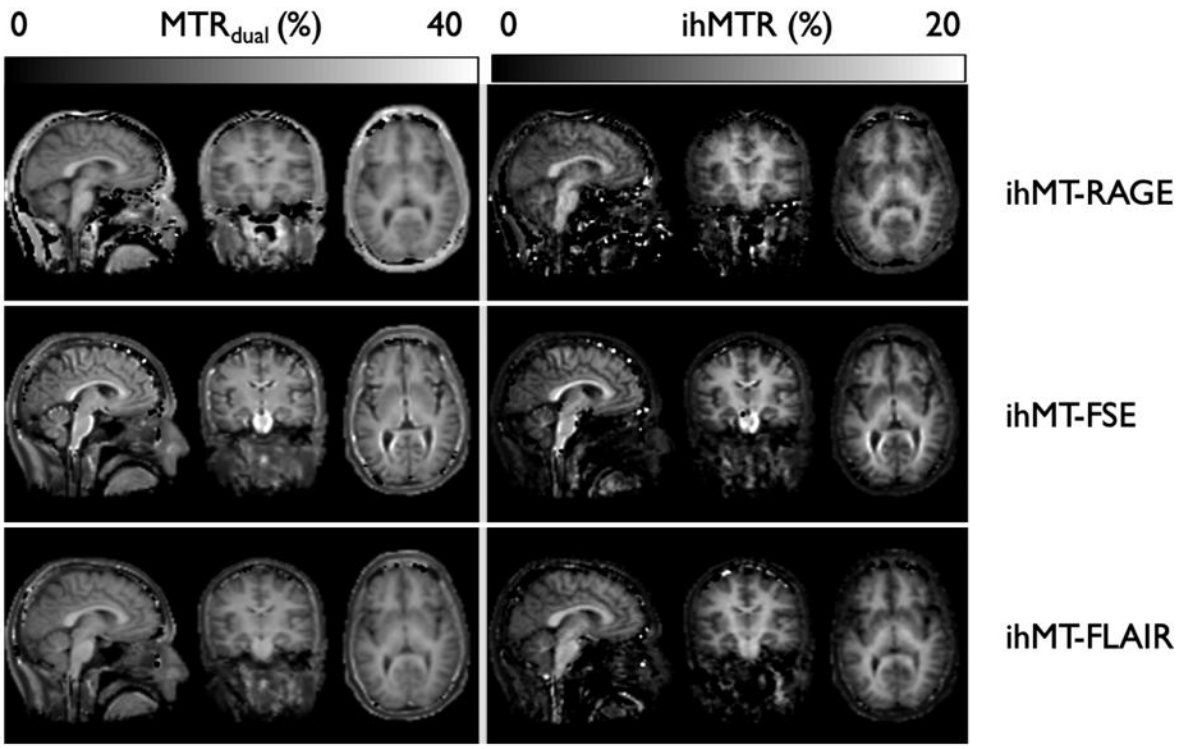

Supporting Information Figure S4 - illustration of single-subject $MTR_{dual}= (M_0-MT_{dual})/M_0$ and ihMTR ($ihMT/M_0$). Images have been masked and spline-interpolated for visualization purposes

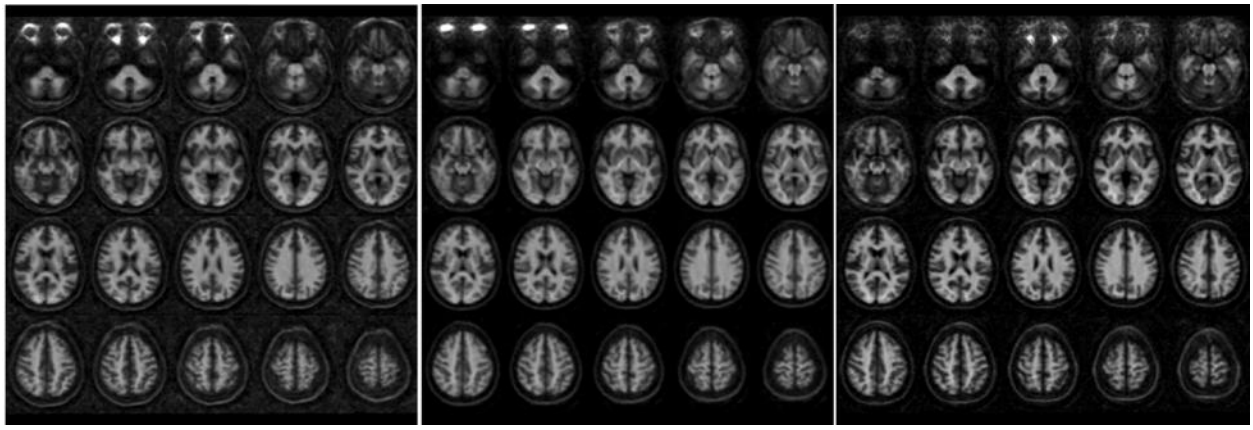

Supporting Information Figure S5 – axial cuts of ihMT-RAGE (left), ihMT-FSE (center) and ihMT-FLAIR (right) differences group averages

Parameter	Gray Matter	White Matter
Free-pool longitudinal relaxation rate R_{1a} (s^{-1})	0.72	1.23
Exchange rate R (s^{-1})	51	60
Bound pool longitudinal relaxation rate R_{1b} (s^{-1})	1	1
Dipolar longitudinal relaxation time T_{1D} (s)	5.90E-03	6.20E-03
Free-pool transverse relaxation time T_{2a} (s)	9.90E-02	6.90E-02
Bound pool transverse relaxation time T_{2b} (s)	7.60E-06	9.00E-06
Free-pool magnetization M_{0A}	1	1
Bound pool fully relaxed magnetization M_{0b}	0.035	0.1

Supporting Information Table S1 – Tissue properties used in numerical simulations